

Development of compressible large-eddy simulations combining high-order schemes and wall modeling

S. Le Bras *

Centre Européen de Recherche et de Formation Avancée en Calcul Scientifique, 31057 Toulouse, France

H. Deniau[†]

ONERA, French Aerospace Lab, 31000 Toulouse, France

C. Bogey[‡]

Laboratoire de Mécanique des Fluides et d'Acoustique, Ecole Centrale de Lyon, 69134 Ecully, France

G. Daviller[§]

IMFT, allée du Professeur Camille Soula, 31400 Toulouse, France.

Compressible Large Eddy-Simulations (LES) combining high-order methods with a wall model have been developed in order to compute wall-bounded flows at high Reynolds numbers. The high-order methods consist of low-dissipation and low-dispersion implicit finite-volume schemes. In a first part, the procedure used to apply these schemes in near-wall regions is presented. This procedure is based on a ghost cell reconstruction. Its validity is assessed by performing the LES of a bi-periodic turbulent channel flow at a Mach number of $M = 0.2$ and a friction Reynolds number of $Re_\tau = 395$. In a second part, to consider flows at higher Reynolds numbers, a LES approach using a wall model is proposed. The coupling between the wall model and the high-order schemes is described. The performance of the approach is evaluated by simulating a bi-periodic turbulent channel flow at $M = 0.2$ and $Re_\tau = 2000$, and an isothermal subsonic round jet at $M = 0.6$ and $Re_D = 5.7 \times 10^5$. The results are in agreement with Direct Numerical Simulation (DNS) data and experimental results. In particular, the turbulent intensities obtained in the logarithmic region of the boundary layers of the channel flow and the jet far-field noise are successfully predicted.

I. Introduction

In computational aeroacoustics, the direct calculation of the acoustic field from the governing equations requires accurate numerical methods to capture noise sources in turbulent flows and to propagate sound waves. Among various approaches available in the literature,¹ Large Eddy Simulations (LES) using high-order, low-dissipation and low-dispersion implicit schemes is an attractive way. In the LES approach, the large structures of the flows are computed whereas the effects of the smallest turbulent scales are taken into account by a subgrid-scale model. Using high-order implicit schemes offers the advantage to resolve the flow over a wide range of length scales using a reduced number of grid points. Currently, LES receives increasing attention for the study of complex turbulent flows. However, for wall-bounded flows at high Reynolds numbers, typically higher than 10^6 , LES requires very fine grids to capture the small but dynamically important turbulent structures developing in the near-wall regions. These constraints on the grid resolution lead to LES computational costs which increase as a power of the Reynolds number.² In these conditions, the simulations are out of reach considering the current numerical resources.

*PhD Student. Corresponding author. *Email address:* lebras@cerfacs.fr

[†]ONERA Research Scientist.

[‡]CNRS Research Scientist.

[§]Postdoctoral Fellow.

This severely limits the applications of LES, especially for flows in the presence of walls with realistic geometries. This is particularly true for turbofan jet flows for which the nozzle geometry plays a fundamental role. Indeed, the jet flow is strongly influenced by the shear layers developing from the nozzle lips. Recent studies have also shown that the initial conditions of the jet at the nozzle exit significantly affect the acoustic results.^{3,4} In particular, the values of the boundary-layer momentum thickness and the turbulence intensity at the nozzle exit must correspond to the experimental conditions. Consequently, taking into account the jet nozzle geometry and ensuring a good resolution of the boundary layers are recommended to obtain reliable predictions of the noise radiated from the jet.

In order to perform LES of wall-bounded flows at high Reynolds numbers without resolving the boundary layers, one solution is to use a wall model. Wall modeling aims to reproduce the variations of the mean flow in the inner part of boundary layers, as illustrated in figure 1 where the inner and the outer regions of a boundary layer are represented. Keeping in mind that to ensure the resolution of a boundary layer at $Re = 10^6$, around 99% of the grid points are located in the inner region,⁵ wall modeling drastically reduces the size of the computational grids. Therefore, LES is performed on coarse grids which do not resolve the near-wall fluctuations, and approximate boundary conditions are provided by the model close to the walls.

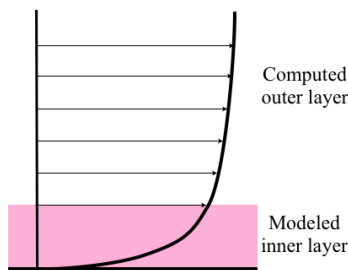


Figure 1. Sketch of the computation of a boundary layer with a wall model.

Wall-Modeled LES (WMLES) and more generally hybrid RANS-LES methods, currently know a great success among the scientific community.⁶ Wall modeling for LES appeared in the seventies thanks to Deardorff's⁷(1970) and Schumann's⁸(1975) works. Since, wall models have been applied to different flow configurations and implemented using several numerical approaches. The quality of LES combining wall models and high-order methods have been examined by many authors. For instance, very promising results have been obtained using finite difference approaches⁹ and spectral difference methods.¹⁰

In the present study, a wall model is combined with 6th-order finite-volume compact schemes in order to perform the LES of wall-bounded flows at high Reynolds numbers. In a previous study, the high-order schemes were validated for an isothermal subsonic jet without studying the flow inside the nozzle.¹¹ In a first part of the present paper, a procedure is proposed to allow the application of the compact schemes at walls. This procedure is validated for a turbulent channel flow at low Reynolds number. In a second part, to deal with flows at higher Reynolds numbers, the analytical compressible wall model developed by Bocquet¹² for LES using finite volume low-order schemes is considered. The combination of this model with the high-order schemes is presented. Its validity is examined for a turbulent channel flow and for an isothermal subsonic jet including a nozzle.

II. Wall-Resolved LES (WRLES)

A. WRLES approach

1. Governing equations

In the present work, the full compressible three-dimensional Navier-Stokes equations are solved using the *elsA* software,¹³ which is a Finite-Volume (FV) multi-block structured solver. In Cartesian coordinates, they can be written as:

$$\frac{\partial \mathbf{U}}{\partial t} + \frac{\partial \mathbf{E}_c}{\partial x} + \frac{\partial \mathbf{F}_c}{\partial y} + \frac{\partial \mathbf{G}_c}{\partial z} - \frac{\partial \mathbf{E}_d}{\partial x} - \frac{\partial \mathbf{F}_d}{\partial y} - \frac{\partial \mathbf{G}_d}{\partial z} = 0 \quad (1)$$

where $\mathbf{U} = (\rho, \rho u, \rho v, \rho w, \rho e)^t$ is the variable vector, (u, v, w) are the velocity components, ρ is the density, ρe represents the total energy, \mathbf{E}_c , \mathbf{F}_c and \mathbf{G}_c are the convective fluxes, and \mathbf{E}_d , \mathbf{F}_d and \mathbf{G}_d are the diffusive fluxes.

The total energy ρe for a perfect gas is defined by:

$$\rho e = \frac{p}{\gamma - 1} + \frac{1}{2}\rho(u^2 + v^2 + w^2) \quad (2)$$

where γ is the specific heat ratio and p is the static pressure. The convective fluxes are given by:

$$\begin{cases} \mathbf{E}_c = (\rho u, \rho u^2 + p, \rho uv, \rho uw, (\rho e + p)u)^t \\ \mathbf{F}_c = (\rho v, \rho uv, \rho v^2 + p, \rho vw, (\rho e + p)v)^t \\ \mathbf{G}_c = (\rho w, \rho uw, \rho vw, \rho w^2 + p, (\rho e + p)w)^t \end{cases} \quad (3)$$

and the diffusive fluxes by:

$$\begin{cases} \mathbf{E}_d = (0, \tau_{11}, \tau_{12}, \tau_{13}, \tau_{11}u + \tau_{12}v + \tau_{13}w + \Phi_1)^t \\ \mathbf{F}_d = (0, \tau_{21}, \tau_{22}, \tau_{23}, \tau_{21}u + \tau_{22}v + \tau_{23}w + \Phi_2)^t \\ \mathbf{G}_d = (0, \tau_{31}, \tau_{32}, \tau_{33}, \tau_{31}u + \tau_{32}v + \tau_{33}w + \Phi_3)^t \end{cases} \quad (4)$$

where $\tau_{i,j}$ is the viscous stress tensor, and $\Phi = (\Phi_1, \Phi_2, \Phi_3)^t$ is the heat flux vector. The viscous stress tensor $\tau_{i,j}$ is defined by $\tau_{i,j} = 2\mu S_{i,j}$, where μ is the dynamic molecular viscosity and $S_{i,j}$ is the deformation stress tensor:

$$S_{i,j} = \frac{1}{2} \left(\frac{\partial u_i}{\partial x_j} + \frac{\partial u_j}{\partial x_i} - \frac{2}{3} \frac{\partial u_k}{\partial x_k} \delta_{i,j} \right) \quad (5)$$

The heat flux vector Φ is computed using Fourier's law, yielding:

$$\Phi = -\lambda \nabla T \quad (6)$$

where ∇T is the temperature gradient, $\lambda = C_p \mu / Pr$ is the thermal conductivity, C_p is the specific heat at constant pressure, and Pr is the Prandtl number.

2. Numerical methods

In the FV approach, the computational domain is partitioned into non-overlapping control volumes $\Omega_{i,j,k}$, where i, j , and k are the volume indexes. For clarity reason, the FV method is presented for the linear convection equation:

$$\frac{\partial \mathbf{U}}{\partial t} + \nabla \cdot \mathbf{f}(\mathbf{U}) = 0 \quad (7)$$

where \mathbf{f} is a linear vectorial function of the variable vector \mathbf{U} . The equation (7) is integrated on the elementary volumes $\Omega_{i,j,k}$, using the divergence theorem:

$$\frac{d}{dt} \int_{\Omega_{i,j,k}} \mathbf{U} dV + \int_{\partial\Omega_{i,j,k}} \mathbf{f}(\mathbf{U}) \cdot \mathbf{n} dS = 0 \quad (8)$$

where $\partial\Omega_{i,j,k}$ represents the faces of $\Omega_{i,j,k}$, and \mathbf{n} is the outgoing unitary normal of $\Omega_{i,j,k}$. Supposing that $\Omega_{i,j,k}$ is an hexahedra and using the linearity of \mathbf{f} , equation (8) is equivalent to:

$$\frac{d}{dt} \int_{\Omega_{i,j,k}} \mathbf{U} dV + \mathbf{f} \left(\int_{\partial\Omega_{i,j,k}} \mathbf{U} dS \right) \cdot \mathbf{n} = 0 \quad (9)$$

Therefore, the computation of the derivatives of the convective fluxes corresponds to the calculation of the fluxes from the averaged value of \mathbf{U} at the cell interfaces. In order to approximate the interface-averaged value of \mathbf{U} , an interpolation is performed using the primitive variables (u, v, w, p, T) . In the following, the quantity q is employed to designate a primitive variable. In addition, the averaged value of q at the interface of the volume $\Omega_{i,j,k}$ is defined as:

$$\tilde{q} = \frac{1}{\partial\Omega_{i,j,k}} \int_{\partial\Omega_{i,j,k}} q dS \quad (10)$$

and the averaged value of q in the volume $\Omega_{i,j,k}$ as:

$$\bar{q} = \frac{1}{\Omega_{i,j,k}} \int_{\Omega_{i,j,k}} q dV \quad (11)$$

In order to obtain a high-order calculation of the convective fluxes derivatives, a high-order interpolation of the values \bar{q} is performed. Considering the one-dimensional computational domain of figure 2, the interpolated value of \bar{q} at the interface $i + 1/2$ is obtained by solving the implicit relation:

$$\alpha_{i+1/2} \bar{q}_{i-1/2} + \bar{q}_{i+1/2} + \beta_{i+1/2} \bar{q}_{i+3/2} = \sum_{l=-1}^2 a_l \bar{q}_{i+l} \quad (12)$$

where $\alpha_{i+1/2}$, $\beta_{i+1/2}$ and a_l are the interpolation coefficients which are determined using 6th-order Taylor series. For a simulation using an uniform Cartesian mesh, Fosso et al.¹⁴ demonstrated that the formulation given by equation (12) is equivalent to Lele's 6th-order implicit compact finite-difference scheme.¹⁵ The effective order of the scheme is between 5 and 6.

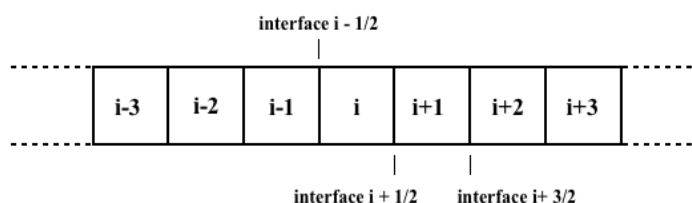


Figure 2. Representation of a one-dimensional computational domain.

As the numerical scheme is based on a centered formulation, the stability of the computations is ensured using the 6th-order compact filter of Visbal & Gaitonde.¹⁶ The filter is applied to the primitive variables to remove grid-to-grid oscillations. It is also used as an implicit subgrid-scale model for LES, relaxing turbulent energy at high frequencies. The filtering operator applies to cell-averaged values, and allows to the filtered values denoted \hat{q} to be estimated from the unfiltered cell-averaged quantities \bar{q} in the following way:

$$\alpha_f \hat{q}_{i-1} + \hat{q}_i + \alpha_f \hat{q}_{i+1} = \sum_{l=-3}^3 \beta_l \bar{q}_{i+l} \quad (13)$$

where α_f is a constant equal to 0.47, and β_l are the filter coefficients.¹⁶

The diffusive fluxes in equation (4) are computed using a 2nd-order method.¹⁷ In this method, the values of the velocity and the temperature gradients are evaluated at the cell interfaces to compute the deformation stress $S_{i,j}$ and the heat flux vector Φ .

Time discretization is performed using a low-storage 6-stage Runge Kutta algorithm of 2nd-order.¹⁸ Radiation boundary conditions and Navier-Stokes characteristic boundary conditions are implemented.¹⁹ A full description of the numerical algorithm and its application to a single jet are available in Fosso et al.²⁰

3. Wall treatment for WRLES

The computation of the convective fluxes is performed using high-order schemes, based on a centered seven-point stencil. Close to the computational boundaries, these schemes cannot be applied. Considering the one-dimensional domain represented in figure 3, the use of the interpolation relation given by equation (12) is not possible to compute the flow variables \bar{q} at the interfaces 1/2 and 3/2. The stencil available is not large enough.

Therefore, a specific methodology is proposed close to the boundaries. This methodology must not affect the stability and the accuracy of the implicit schemes. Such near-wall discretizations have been largely studied for finite-difference schemes.^{21,22} However, to our knowledge, no formulation is available in FV. Therefore, a new FV boundary discretization is presented here. A simple way to proceed is to directly impose the boundary condition $\bar{q}_{1/2}$ at the wall, and to apply a non-centered scheme to compute the interface 3/2:

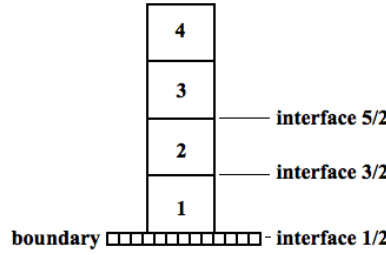


Figure 3. One-dimensional computational domain close to a boundary. The computational cells are numbered 1, 2, 3 and 4, and the interfaces 1/2, 3/2 and 5/2. The interface 1/2 represents the boundary interface.

$$\alpha'_{3/2}\tilde{q}_{1/2} + \tilde{q}_{3/2} + \beta'_{3/2}\tilde{q}_{5/2} = \sum_{l=1}^4 a'_l \bar{q}_l \quad (14)$$

where $\alpha'_{3/2}$, $\beta'_{3/2}$ and a'_l are the scheme coefficients. Unfortunately, when applied near the walls, this discretization leads to numerical oscillations. It might be due to the fact that for a wall, various boundary conditions are imposed to the different flow variables. Indeed, it is not always possible to explicitly impose a value for $\tilde{q}_{1/2}$ at the wall interface. More precisely, the velocity satisfies a Dirichlet condition at the wall, leading to a velocity equal to zero. In this case, the value $\tilde{q}_{1/2} = 0$ can be imposed at the wall. However, the pressure follows a Neumann condition, yielding a zero wall-normal pressure gradient. The temperature is characterized by a Neumann condition in the case of an adiabatic wall, whereas a Dirichlet condition is considered for an isothermal wall. In order to obtain a value of $\tilde{q}_{1/2}$ from a Neumann condition dq/dn , an additional discretization scheme is needed, which can deteriorate the stability of the scheme in equation (12). To bypass this issue, the wall boundary conditions are not explicitly imposed. Instead, the primitive variables at the wall interface are reconstructed to impose an adiabatic or an isothermal condition at the wall. For this purpose, the size of the computational domain is extended introducing ghost cells, as illustrated in figure 4 where the ghost cells are numbered 0, -1 and -2.

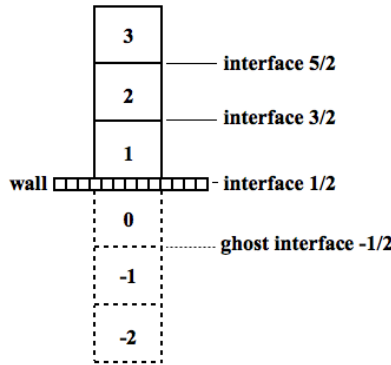


Figure 4. Extended one-dimensional computational domain close to a wall. The cells numbered -2, -1 and 0 are ghost cells. The cells 1, 2, 3 are "real" cells. The interface 1/2 is the boundary interface of the domain.

Three rows of ghost cells allow the scheme of Fosso et al. and the filter to be applied down to the wall. To prescribe the desired conditions at the wall, the values in the ghost cells are specified using first order relations:

$$\begin{aligned} \bar{q}_0 &= f(\bar{q}_1) \\ \bar{q}_{-1} &= f(\bar{q}_2) \\ \bar{q}_{-2} &= f(\bar{q}_3) \end{aligned} \quad (15)$$

where the function f depends on the variable q and on the wall conditions. In particular, f is defined as $f = -I_d$ for the velocity components, where I_d is the identity function. The function f is equal to I_d for

the temperature for an adiabatic wall and for the pressure. Moreover, f corresponds to $2T_w - I_d$ for the temperature in the case of an isothermal wall, where T_w is the wall temperature. Then, equation (12) is solved to interpolate the flow variables at the interfaces 3/2 and 1/2. For this purpose, a ghost interface, numbered $-1/2$ in figure 4, is introduced using the function f :

$$\tilde{q}_{-1/2} = f(\tilde{q}_{3/2}) \quad (16)$$

For the filter, a similar technique is employed. In addition, a ghost filtered value is introduced to apply the equation (13) at the point 1 above the wall:

$$\hat{q}_0 = f(\hat{q}_1) \quad (17)$$

The stability and the accuracy of the numerical algorithm is now evaluated for a turbulent channel flow.

B. Turbulent channel flow

A three-dimensional turbulent channel flow has been computed using the wall discretization described above. The flow is characterized by Mach number of $M = U_b/c = 0.2$ and a friction Reynolds number of $Re_\tau = u_\tau h/\nu_w = 391$, where c is the sound speed, u_τ is the friction velocity at the wall, h is the channel half height, ν_w is the kinematic molecular viscosity at the wall, and U_b is the bulk velocity defined as:

$$U_b = \frac{1}{h} \int_0^h u(y) dy \quad (18)$$

Similar channel flows have been simulated at $Re_\tau = 395$ by Abe et al.²³ and Moser et al.,²⁴ using Direct Numerical Simulation (DNS). In the following, the streamwise, the wall-normal and the spanwise spatial coordinates are denoted x , y and z . The channel lengths are equal to $L_x = 2\pi h$, $L_y = 2h$ and $L_z = \pi h$, as in the DNS.²⁵ At the top and the bottom channel walls, adiabatic boundary conditions are imposed. Periodic boundary conditions are applied in the streamwise and spanwise directions. In order to compensate the effects of the viscous dissipation and thus impose the flow regime, a source term, in the form of a pressure gradient, is introduced in the streamwise momentum equation.²⁶ For the simulation, the mesh has been designed to satisfy the constraints generally prescribed for LES. The grid parameters, namely the numbers of mesh points in each direction n_x , n_y and n_z as well as the streamwise, normal and spanwise grid spacings Δx^+ , Δy^+ and Δz^+ , are given in table 1.

	$n_x \times n_y \times n_z$	Δx^+	Δz^+	Δy_w^+	Δy_{max}^+
Wall-resolved LES	$161 \times 181 \times 121$	15	10	1	8

Table 1. Grid parameters used for the WRLES of the channel flow at $Re_\tau = 395$.

The grid contains 3.5 million points. The mesh spacings Δ^+ are scaled by the viscous length $y_\tau = \nu_w/u_\tau$. The streamwise and the spanwise grid spacings Δx^+ and Δz^+ are uniform, and the minimum and the maximum wall-normal mesh spacings are respectively equal to $\Delta y_w^+ = 1$ at the wall and $\Delta y_{max}^+ = 8$ at the center of the channel. The time step Δt for the simulation is chosen so that $CFL = c\Delta t/\Delta y_w \simeq 0.7$ to ensure the stability of the time integration. At the initial time $t = 0$, an analytical turbulent velocity profile is imposed in the channel. The transition towards turbulence is accelerated by adding perturbations in the form of spanwise vortices²⁷ to the initial flow field at $t = 0$. The transient period of the simulation lasts during the non-dimensional time period $t^* = tU_b/h = 102$ which is equivalent to 15 flow passings through the channel. The statistics are then collected during a time period $t^* = 102$. The results are averaged in time and in space in the homogeneous directions x and z , and compared to the DNS data.^{23,24}

The main flow parameters, including the Mach number M , the friction Reynolds number Re_τ and the friction coefficient $C_f = 2\tau_w/(\rho_b U_b^2)$ are provided in table 2, where ρ_b is the bulk density and τ_w is the wall shear stress. The value of C_f is estimated with a difference lower than 6%, compared to the DNS friction coefficient $C_f = 6.23 \times 10^{-3}$.

The mean longitudinal velocity profile in wall units $u^+ = \langle u \rangle / u_\tau$ is depicted as a function of the wall distance y^+ in figure 5. The agreement with the DNS is satisfactory in the inner boundary layer between the wall and $y^+ = 20$. From $y^+ = 20$ to $y^+ = 100$, a small discrepancy for the LES is observed. The rms profiles

M	Re_τ	C_f
0.2	391	5.86×10^{-3}

Table 2. Mach number M_c , friction Reynolds number Re_τ and friction coefficient C_f in the channel.

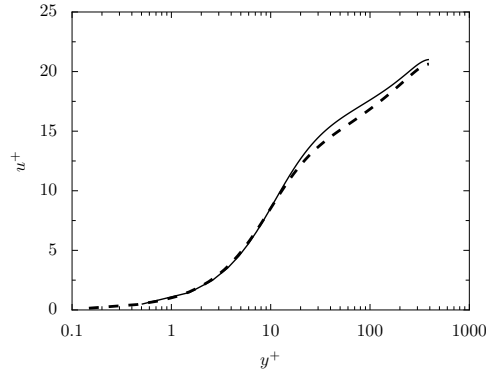


Figure 5. Representation of the mean streamwise velocity in the channel as a function of the wall distance using wall units, — from the WRLES and --- from the DNS of Abe et al.²³

for the velocity components $u'^+ = \langle u'u' \rangle^{1/2} / u_\tau$, $v'^+ = \langle v'v' \rangle^{1/2} / u_\tau$, $w'^+ = \langle w'w' \rangle^{1/2} / u_\tau$ and for the pressure $p'^+ = \langle p'p' \rangle^{1/2} / (\rho_w u_\tau^2)$ are represented in wall units in figure 6, where ρ_w is the density at the wall. For v'^+ , w'^+ and p'^+ , the results are close to the DNS data. For the streamwise fluctuating velocity u'^+ , the position of the peak is well-captured but its intensity is slightly overestimated.

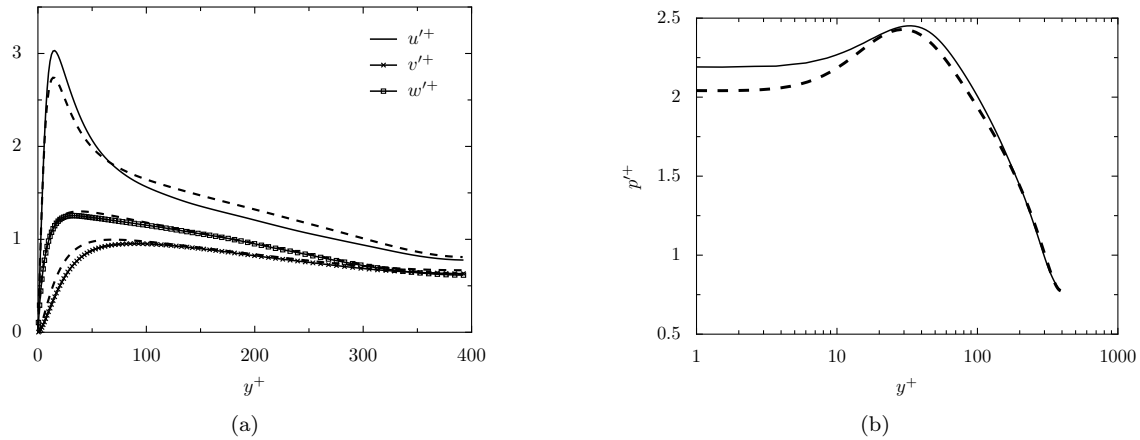


Figure 6. Representation of the root mean square profiles in the channel: (a) the streamwise, the wall-normal and the spanwise velocity components, (b) the pressure, and --- DNS results of Abe et al.²³ as a function of the wall distance using wall units.

The total shear stress, which is the sum of the mean viscous stress $\langle \mu \rangle \langle du/dy \rangle$ and the mean Reynolds stress $-\langle \rho \rangle \langle wv' \rangle$, is displayed in figure 7. The LES results show a good agreement with the DNS. Near the wall, the viscous constraints predominate. For $y/h > 0.04$, corresponding to $y^+ > 15$, the Reynolds stress is higher than the viscous stress, and is nearly equal to the total shear stress for $y/h > 0.2$. Finally, Q-criterion isosurfaces colored by the streamwise velocity magnitude from green to red are presented in figure 8. Two kinds of boundary layer structures appear in the channel. In the near-wall regions, elongated structures named streaks are found. They are represented in green in figure 8, indicating that they are convected at a low velocity. Further from the walls, larger structures, colored in red and thus more rapidly convected, dominate.

These results demonstrate the capability of the present numerical algorithm to deal with wall-bounded flows at low Reynolds numbers.

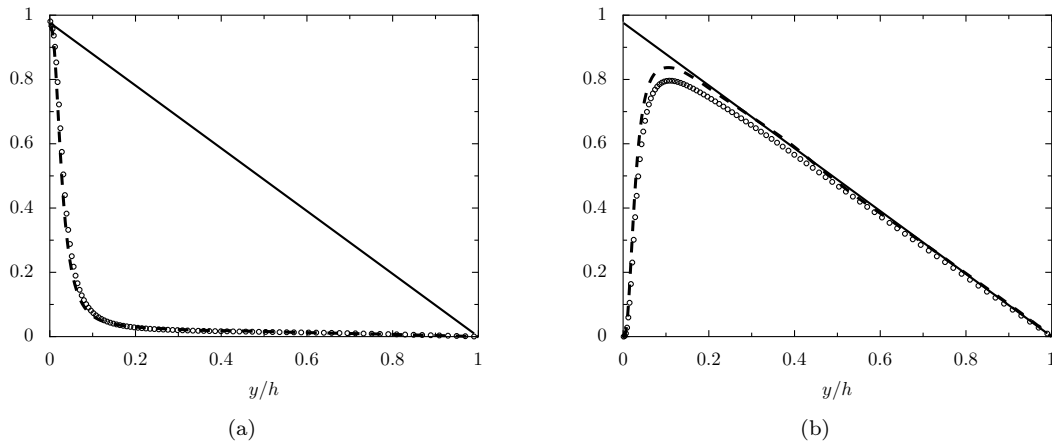


Figure 7. Representation of the shear stress profiles in the channel normalized by the wall shear stress τ_w : from the LES for — the total shear stress $\tau = \langle \mu \rangle \langle du/dy \rangle - \langle \rho \rangle \langle uv' \rangle$, (a) $\circ \circ \circ$ the viscous shear $\langle \mu \rangle \langle du/dy \rangle$, (b) $\circ \circ \circ$ the Reynolds shear stress $-\langle \rho \rangle \langle uv' \rangle$, and --- from the DNS results of Moser et al.,²⁴ as a function of the wall distance y normalized by the channel half height h .

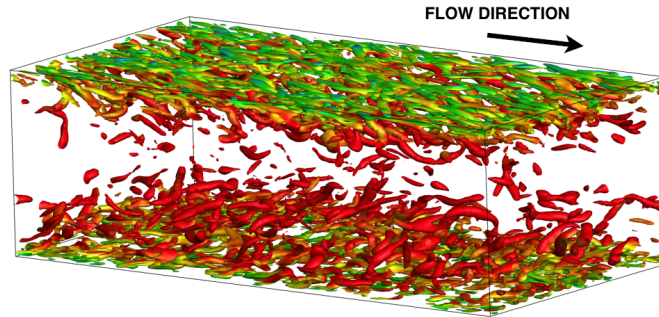


Figure 8. Q-criterion isosurfaces in the channel colored by the streamwise velocity magnitude between 0 and U_b .

III. Wall-Modeled LES (WMLES)

A. WMLES approach

1. Description

When a wall model is used to compute a wall-bounded flow, the inner part of the boundary layers close to the wall is simulated without resolving numerically the turbulent structures developing in this region, as represented in figure 9. A coarser mesh is used near the wall, compared to a simulation where this region is resolved. As mentioned above, in the FV approach, the convective and the diffusive fluxes must be evaluated at the wall interface. The convective fluxes at the wall are determined by imposing an adherence condition and a wall-normal pressure gradient equal to zero. For the computation of the diffusive fluxes, the values of velocity and temperature gradients at the wall are needed. For a simulation using a coarse mesh in the near-wall region, these gradients are not computed accurately by the numerical schemes. Consequently, they must be obtained using a wall model. In practice, the model allows the wall shear stress τ_w and the wall heat flux Φ_w to be estimated. These two quantities are then directly used to calculate the diffusive fluxes at the wall.

The wall model¹² used here relies on Reichardt's²⁸ and Kader's²⁹ analytical laws. The first one allows the mean velocity U to be estimated as a function of the height y above the wall. In wall units, one gets:

$$u^+ = \frac{U}{u_\tau} = \frac{1}{\kappa} \ln(1 + \kappa y^+) + \left(B - \frac{1}{\kappa} \ln \kappa \right) \left(1 - \exp\left(-\frac{y^+}{11}\right) - \frac{y^+}{11} \exp(-0.33y^+) \right) \quad (19)$$

where $y^+ = \rho_w u_\tau y / \mu_w$, μ_w is the dynamic molecular viscosity at the wall, κ is the Von Karman constant equal to 0.41 and B is a constant equal to 5.25. The Kader law approximates the variations of the temperature

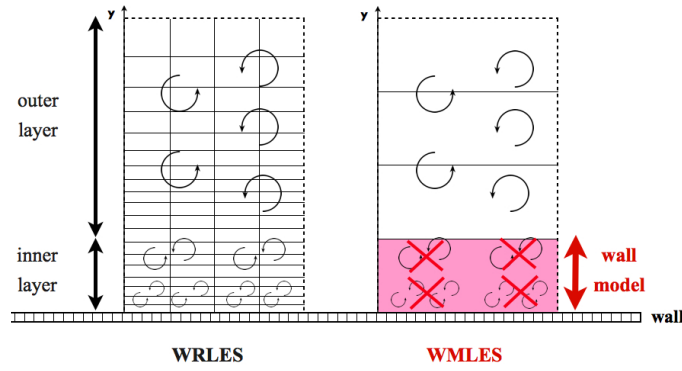


Figure 9. Sketch of the computational grids and the turbulence resolution for WRLES and WMLES.

T as, in wall units:

$$T^+ = -\frac{(T - T_w)\rho_w C_p u_\tau}{\Phi_w} = Pr y^+ \exp(\Gamma) + \left(2.12 \ln(1 + y^+) + (3.85 Pr^{1/3} - 1.3)^2 + 2.12 \ln Pr\right) \exp\left(\frac{1}{\Gamma}\right) \quad (20)$$

where Γ is defined as:

$$\Gamma = -\frac{10^{-2}(Pr y^+)^4}{1 + 5Pr^3 y^+} \quad (21)$$

Equations (19) and (20) have been established for incompressible flows, assuming weak pressure gradients in the streamwise direction. The validity of these wall laws can be extended to compressible flows thanks to the Van Driest's transformation.³⁰

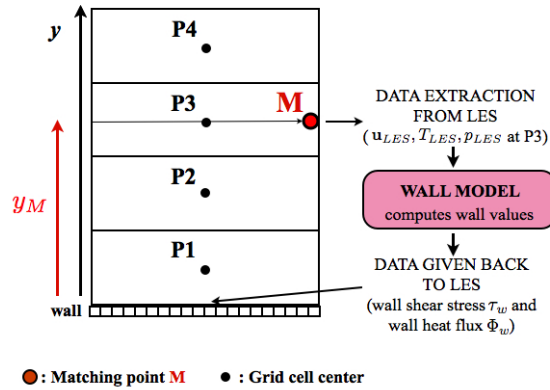


Figure 10. Wall model application. The grid cell centers are numbered from 1 to 4, y represents the distance from the wall. The wall shear stress τ_w and the wall heat flux Φ_w are computed by the model using the instantaneous LES data at the matching point M located at $y = y_M$. The point $P3$ is the matching point in this case.

The procedure used to compute (τ_w, Φ_w) from Kader's and Reichardt's laws is now presented. In order to apply these laws, according to equations (19) and (20), the values of the velocity U and the temperature T , as well as the wall components T_w , μ_w and ρ_w are needed. In order to determine these quantities, the instantaneous LES variables \mathbf{u}_{LES} , T_{LES} and p_{LES} , taken at a computational point M located at a distance y_M from the wall, are considered. This point M , also named the matching point,⁹ is represented in figure 10. The point M must be chosen among the computational points located along the wall-normal direction in the inner part of the boundary layer, such that the conditions of application of the wall laws are verified. For example, in figure 10, the point $P3$ is selected among the potential candidates $P1$, $P2$, $P3$ and $P4$. The position of the matching point will be discussed in section III.A.3. The scalar velocity value U is thus computed by projecting the velocity vector \mathbf{u}_{LES} on the wall:

$$U = \mathbf{u}_{LES} \cdot \mathbf{x}' \quad (22)$$

where \mathbf{x}' is a unitary vector, orthogonal to the wall-normal direction \mathbf{n} and aligned with the flow direction, defined as:

$$\mathbf{x}' = \frac{\mathbf{u}_{LES} - (\mathbf{u}_{LES} \cdot \mathbf{n})\mathbf{n}}{\|\mathbf{u}_{LES} - (\mathbf{u}_{LES} \cdot \mathbf{n})\mathbf{n}\|} \quad (23)$$

where $\|\cdot\|$ is the Euclidean norm.

From this point, the wall modeling procedure differs depending on the isothermal or the adiabatic nature of the wall. In the case of an isothermal wall, the temperature T_w is known at the wall interface. Therefore, the dynamic viscosity at the wall μ_w is computed from Sutherland's law and T_w . In addition, the wall density ρ_w is obtained using the perfect gas equation and assuming a constant pressure along the wall normal direction:

$$\rho_w = \frac{p_{LES}}{RT_w} \quad (24)$$

where R is the perfect gas constant. The friction velocity u_τ is then estimated from the value of U and Reichardt's law, using a Newton algorithm to solve equation (19). Finally, the wall shear stress $\tau_w = \rho_w u_\tau^2$ is computed and the wall heat flux Φ_w is obtained from Kader's law and $T = T_{LES}$. In the case of an adiabatic wall, the value of Φ_w is equal to zero, leading to $T_w = T_{LES}$. The wall shear stress τ_w is then computed in the same way as for an isothermal wall.

2. Implementation with high-order numerical schemes

In the computation of the convective fluxes, in order to apply the seven-point stencil schemes down to the wall, a new spatial discretization has been developed for WMLES. The variables considered for WMLES are u , v , w , p and T . As for WRLES, the wall discretization is different depending on the adiabatic or the isothermal nature of the wall. For an adiabatic wall, the WRLES discretization at the wall is used for the pressure and the temperature components. For an isothermal wall, only the pressure is computed in this way. For the other variables, including the velocity components u , v , w as well as T for an isothermal wall, the wall discretization for WMLES is different. More precisely, for the scheme of Fosso *et al.*,¹⁴ the objective remains to compute the flow variables \tilde{q} at the interfaces 1/2 and 3/2, according to figure 4. With this aim in view, a no-slip condition leading to a velocity equal to zero, and the wall temperature T_w are directly imposed at the wall interface. In addition, the interface $i = 3/2$ is computed using a 2nd-order centered scheme:

$$\tilde{q}_{3/2} = \alpha''_{3/2}\tilde{q}_1 + \beta''_{3/2}\tilde{q}_2 \quad (25)$$

where $\alpha''_{3/2}$ and $\beta''_{3/2}$ are the interpolation coefficients, determined using 2nd-order Taylor series. No ghost cell is needed in this case.

Then, for the filter given by equation (13), three rows of ghost cells are introduced to allow the seven-point stencil formulation to be applied down to the first point from the wall. In this case, the wall model is used to compute the values of the variables u , v , w , and T for an isothermal wall in the ghost cells. The ghost cell reconstruction is depicted for the velocity in figure 11, where the point P1 represents the center of the adjacent cell to the wall. More precisely, this reconstruction is performed in three stages. In a first step, the positions of the ghost cells are specified. The ghost cells lie between the wall and the point P1. They are numbered 0, -1 and -2. Their positions y_i $-2 \leq i \leq 0$ are defined as $y_i = h_1/d_i$, where h_1 is the distance between the wall and the point P1, and d_i is respectively equal to 1.3, 1.5 and 2 for the ghost cells 0, -1 and -2. The influence of the ghost cell locations has not been studied here and the values of d_i are thus arbitrarily chosen. In a second step, the wall shear stress τ_w is determined from Reichardt's law and the LES data at the matching point M. This step has been described in the previous section. Note that the matching point M is not systematically the point P1. In figure 11, it corresponds to a point located further from the wall. Once the value of τ_w is obtained, Reichardt's law provides an analytical profile for the mean velocity U as a function of the wall distance y , as shown in red line in figure 11. In a third and last step, this profile is used to interpolate the values of the mean velocity U_i $-2 \leq i \leq 0$ in the ghost cells. A similar reconstruction to determine the temperature in the ghost cells is performed using Kader's law. The velocity vectors \mathbf{u}_i $-2 \leq i \leq 0$ in the ghost cells are assumed to be collinear with the velocity vector \mathbf{u}_1 at the point P1, and are computed from the values U_i as:

$$\mathbf{u}_i = U_i \frac{\mathbf{u}_1}{\|\mathbf{u}_1\|} \quad (26)$$

Besides, in order to apply the implicit filter given by equation (13) at the point P1, a filtered ghost cell value \hat{q}_0 is needed. For WMLES, the values in the ghost cells are not filtered, leading to the approximation $\hat{q}_0 = \bar{q}_0$.

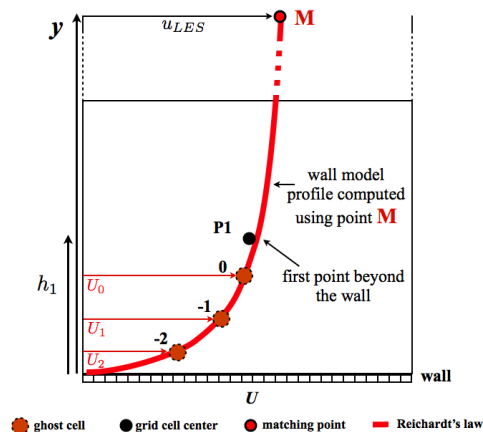


Figure 11. Ghost cell reconstruction for the velocity using Reichardt's law. The ghost cells are represented by red points and indexed: 0, -1, -2. The ghost cell heights are defined using the distance h_1 between the wall and the first point above the wall P1.

3. Matching point location

In the WMLES approach, data are exchanged between the wall model and the LES solver. On the one hand, instantaneous LES values are used to determine the wall shear stress τ_w and the wall heat flux Φ_w from the wall laws. On the other hand, the values of τ_w and Φ_w are used as boundary conditions in the LES approach, and the wall model is involved in the computation of the ghost cell values. In this data exchange, the matching point M, represented in figures 10 and 11, plays a considerable role as it provides the instantaneous LES data used to estimate the values of τ_w and Φ_w . Usually, this point corresponds to the first computational point P1 above the wall. However, recent works^{9,31} demonstrated that a matching point located further from the wall improves the LES results. Two reasons for that can be pointed out. First, the smallest turbulent structures captured by a mesh are necessarily under-resolved because there are not enough grid points to discretize them. Since these small structures have a major influence on the development of the flow in the near-wall region, the LES flow field is not accurately computed at the first computational points above the wall. Secondly, as presented previously, the high-order spatial discretization used for LES must generally be adapted when approaching the wall, leading to numerical errors in this region. Consequently, with a matching point located further from the wall, a better resolution of the turbulent structures at this point should be obtained, and weaker effects of the wall numerical discretization can be expected. Hence, the wall conditions (τ_w , Φ_w) should be estimated more accurately. This is why in figure 10, the point P3 is chosen to be the matching point. The influence of that choice will be investigated in section III.B. The performance of the WMLES approach is now examined for a turbulent channel flow.

B. Turbulent channel flows

1. Parameters

The turbulent channel flow at a Mach number of $M = 0.2$ and a friction Reynolds number of $Re_\tau \simeq 2000$ considered by Hoyas and Jiménez³² using DNS is computed using WMLES. At the walls, adiabatic or isothermal boundary conditions are used. For an isothermal wall, a temperature gradient is introduced by imposing $T_b/T_w = 1.1$, where T_b is the bulk temperature defined as:

$$T_b = \frac{1}{h} \int_0^h T(y) dy \quad (27)$$

In order to impose a constant mass flow rate and the bulk temperature in the channel, source terms are introduced in the streamwise momentum equation and in the energy equation.²⁶ The streamwise, normal

and spanwise lengths of the channel L_x , L_y and L_z are respectively equal to $2\pi h$, $2h$ and πh . Two uniform Cartesian meshes, a coarse one M1 and a refined one M2, are used. The grid parameters, including the numbers of mesh points n_x , n_y and n_z in each direction as well as the different grid spacings Δ^+ , are provided in table 3. The mesh that would be needed to perform a WRLES of the present flow is also given.

	$n_x \times n_y \times n_z$	Δx^+	Δz^+	Δy_w^+	Δy_{max}^+
WMLES M1	$49 \times 41 \times 41$	261	157	100	100
WMLES M2	$153 \times 67 \times 101$	82	62	60	60
Estimated wall-resolved LES	$840 \times 630 \times 630$	15	10	1	8

Table 3. Grid parameters used for the WMLES of the channel flow at $Re_\tau = 2000$. The estimations for a wall-resolved LES (WRLES) are also provided.

The mesh M1 was designed to satisfy the grid recommendations for WMLES.¹² The grid cells are chosen to capture the large turbulent structures in the outer region of the boundary layers, for $y^+ > 100$, which are elongated in the streamwise direction. Therefore, the grid spacings in the streamwise, normal and spanwise directions are respectively equal to 260, 100 and 160. Thus, the mesh M1 contains 80,000 points. The mesh M2 is finer than M1, and was built to obtain grid spacings Δ^+ between 60 and 80 in all directions. It contains 1 million points. Compared to the grid size estimations for WRLES given in table 3, the WMLES mesh size is 4,000 times smaller using mesh M1 and 300 times smaller using mesh M2.

The performance of WMLES is evaluated by performing eight channel flow simulations depending on the use of adiabatic or isothermal walls, of the mesh M1 or M2, and of different matching points M located at a height y_M^+ from the wall (see in table 4). In order to study the influence of the matching point location, the value of y_M^+ varies between 30 and 250. In particular, in the different simulations, the matching point is either the first point from the wall P1, or the third point P3. Note that the position of the matching point y_M^+ depends on the resolution of the mesh. For instance, the point P1 is located at $y_M^+ = 50$ for the mesh M1, whereas its position is at $y_M^+ = 30$ for the mesh M2.

simulation	wall nature	mesh	matching point M	y_M^+
A-M1P1	adiabatic	M1	P1	50
A-M1P3	adiabatic	M1	P3	250
A-M2P1	adiabatic	M2	P1	30
A-M2P3	adiabatic	M2	P3	150
I-M1P1	isothermal	M1	P1	50
I-M1P3	isothermal	M1	P3	250
I-M2P1	isothermal	M2	P1	30
I-M2P3	isothermal	M2	P3	150

Table 4. Channel flow parameters for WMLES, where y_M^+ represents the matching point position from the wall normalized in wall units.

For the simulations, the time step is chosen such that $CFL = c\Delta t/\Delta y \simeq 0.7$. The simulation transient period lasts during the non-dimensional time $t^* = tU_b/h = 200$, corresponding to 30 flow passings through the channel. Then, the statistics are sampled over 30 flow passings. The results are averaged in time and in space, and compared with the values of the DNS of Hoyas and Jiménez.³² In the case of isothermal walls, the WMLES temperature profiles are compared to the profile given by Kader's law.²⁹

2. Results for adiabatic walls

The flow parameters for the channels with adiabatic walls, including the Mach number M and the bulk friction coefficient C_f , are presented in table 5. For all simulations, the Mach number is equal to 0.2. The friction coefficients are compared to the DNS value of $C_f = 4.2 \times 10^{-3}$. The poorest agreement is obtained for the simulations using the matching point P1. The LES performed using the refined mesh M2 and the matching point P3 provides the best estimations of C_f . For both meshes, choosing the matching point P3 reduces the difference with the DNS value of C_f , as expected in the previous discussion in section III.A.

simulation	M	C_f
A-M1P1	0.20	4.6×10^{-3}
A-M1P3	0.20	4.3×10^{-3}
A-M2P1	0.20	4.6×10^{-3}
A-M2P3	0.20	4.2×10^{-3}

Table 5. Mach number M , friction Reynolds number Re_τ and friction coefficient C_f in the channel for simulations with adiabatic walls.

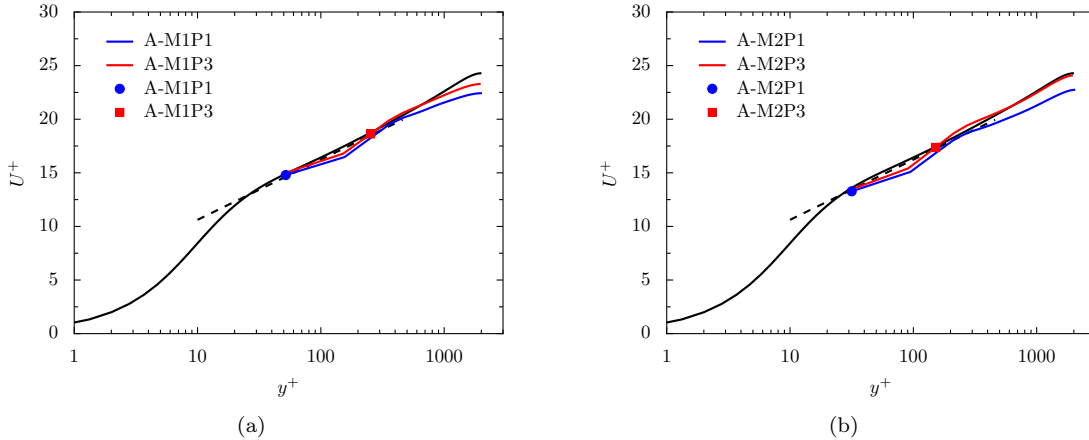


Figure 12. Representation of the mean streamwise velocity obtained from the WMLES for adiabatic walls using (a) the mesh M1 and (b) the mesh M2, using the matching point — P1 and — P3; — from the DNS of Hoyas and Jiménez,³² and - - - from the logarithmic law, as a function of the wall distance using wall units. The symbols represent the positions of the matching point.

The mean longitudinal velocity profiles obtained from the simulations with adiabatic walls are depicted in figure 12. The matching points are represented using symbols, and are located in the logarithmic region of the boundary layer between $y^+ = 30$ and $y^+ = 250$. They match with the wall law represented in dashed line, as expected from the definition of the matching point given in section III.A. The influence of the matching point position for the LES using the mesh M1 and the mesh M2 is illustrated in figures 12(a) and 12(b) respectively. Defining the matching point as the third off-wall point P3 improves the LES results. One possible reason is that the flow field is better resolved by LES for the points located far from the wall, as related in section III.A. The LES using the refined mesh M2 and the matching point P3 provides the best agreement with the DNS data. Two main reasons may explain this result. First, the turbulent structures of the outer part of the boundary layer are better captured when the mesh resolution increases, and a better performance of wall modeling can thus be expected. Secondly, when the mesh is refined, selecting the matching point P3 allows to impose $y_M^+ = 150$ to respect the WMLES recommendations. One can remark that, in the literature, when the matching point P3 is chosen, the velocity at the points located between the wall and the point P3 does not always follow the wall law.³¹ In the present study, the point P1 remains on the wall law profile. This may be due to the ghost cell reconstruction combined with the seven-point stencil filter applied at the point P1.

The root mean square velocity fluctuations u'^+ , v'^+ , w'^+ are represented in wall units for the WMLES using the mesh M1 and the mesh M2 in figures 13 and 14 respectively. Better results are obtained when the matching point is the point P3. In particular, higher turbulent levels for all the rms components, especially in the logarithmic region between $y^+ = 200$ and $y^+ = 500$, are found. For the LES using the mesh M1, the differences with respect to the DNS are stronger than for the simulations using the mesh M2. This may be attributed to the low resolution of the grid M1. For the LES using the mesh M2, the results obtained for the wall-normal velocity v'^+ and the spanwise velocity w'^+ agree well with DNS when the matching point is P3. However, the streamwise fluctuating velocity u'^+ still falls below the DNS profile for $y^+ > 300$.

Finally, the turbulent kinematic constraints $-uv'^+$ are displayed for the WMLES using the mesh M1 in figure 15(a) and the mesh M2 in figure 15(b). The computational cell centers are represented using symbols in the figures. Once again, the best agreement with DNS is obtained when the matching point is the point

P3. Increasing the mesh resolution also leads to higher turbulent levels. In particular, for the LES using the refined mesh M2, the turbulent kinematic constraints match with the DNS values from the point P3 in figure 15(b). This demonstrates that the turbulence is better resolved in this simulation. For the LES using the coarse mesh M1, some discrepancies with the DNS data are observed, even if the matching point P3 is used. These results highlight the advantages to consider a matching point relatively far from the wall and to pay attention to the resolution of the mesh used for WMLES.

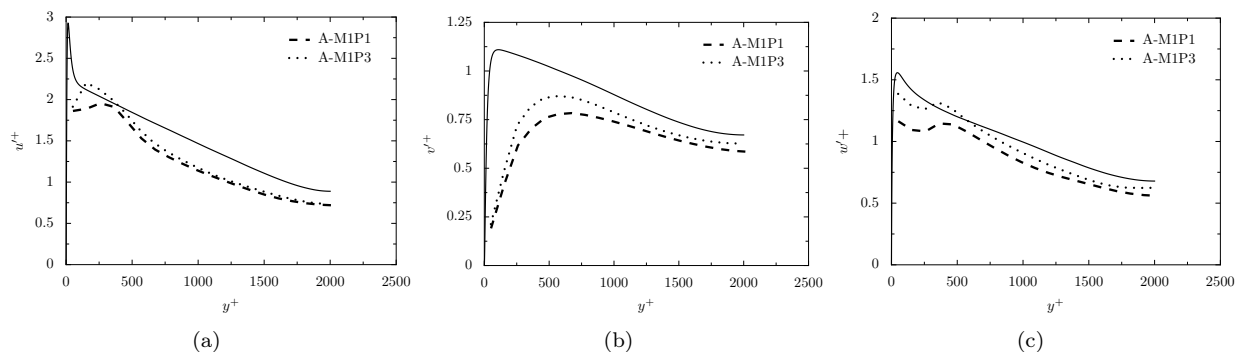


Figure 13. Representation of the rms velocity fluctuations obtained from WMLES for adiabatic walls using the mesh M1 for (a) the streamwise, (b) the wall-normal and (c) the spanwise components, using the matching point --- P1, ---- P3, and from — the DNS of Hoyas and Jiménez,³² as a function of the wall distance using wall units.

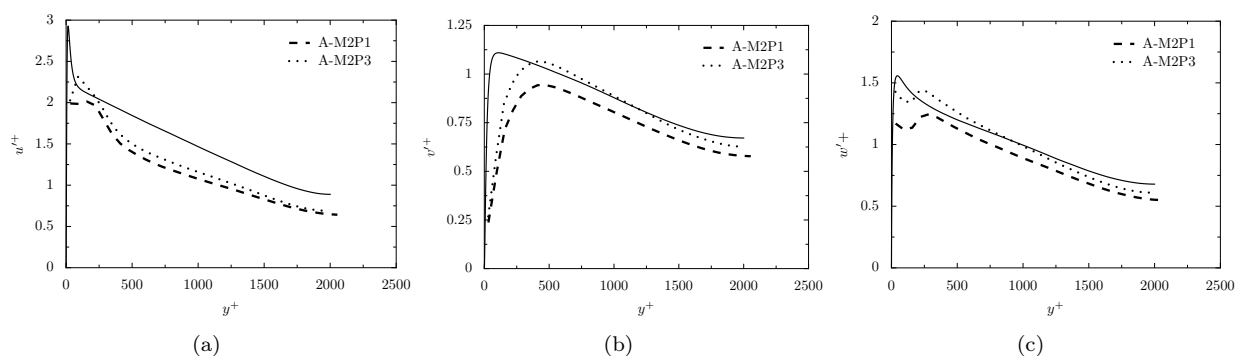


Figure 14. Representation of the rms velocity fluctuations obtained from WMLES for adiabatic walls using the mesh M2 for (a) the streamwise, (b) the wall-normal and (c) the spanwise components, using the matching point --- P1, ---- P3, and from — the DNS of Hoyas and Jiménez,³² as a function of the wall distance using wall units.

3. Results for isothermal walls

For the simulations including isothermal walls, no DNS data are available. Nevertheless, the channel flow is simulated at a low Mach number and the temperature gradient at the wall is sufficiently weak to consider the temperature as a passive scalar. The flow regime is said to be quasi-incompressible in this case. As a consequence, the LES friction coefficient C_f should not be significantly influenced by the small temperature gradient and can be compared to the DNS coefficient $C_f = 4.2 \times 10^{-3}$ obtained for adiabatic walls. The friction coefficient estimated from the empirical correlation of Petukhov³³ equal to $C_f = 4.0 \times 10^{-3}$ is also used for comparisons. The Mach number and the friction coefficient C_f obtained from LES are presented in table 6. The Mach number is close to 0.2 for all simulations. Compared to the LES with adiabatic walls, slightly higher values of C_f are obtained. The simulation using the refined mesh M2 and the matching point P3 still provides the best estimations.

The mean velocity profiles obtained from WMLES are depicted in figure 16 as functions of the wall distance. They are compared with DNS results of Hoyas and Jiménez,³² and to the profile given by Reichardt's law computed from the friction coefficient provided by the correlation of Petukhov.³³ Note that the velocity profiles obtained from the DNS and from the wall law are similar, except for the wake region at $y^+ > 10^3$. The WMLES results are close to those obtained for the simulations including adiabatic walls in figure 12,

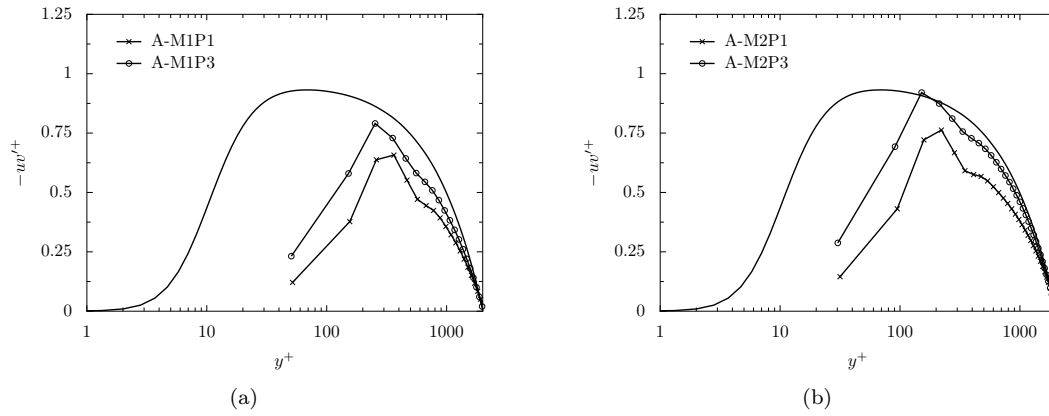


Figure 15. Representation of the turbulent kinematic constraints obtained from WMLES for adiabatic walls, using (a) the mesh M1, (b) the mesh M2, and using the matching point \times P1, \circ P3, and — from the DNS of Hoyas and Jiménez,³² as a function of the wall distance using wall units. The symbols represent the computational cell centers.

simulation	M	C_f
I-M1P1	0.22	4.7×10^{-3}
I-M1P3	0.21	4.6×10^{-3}
I-M2P1	0.21	4.8×10^{-3}
I-M2P3	0.20	4.5×10^{-3}

Table 6. Mach number M and friction coefficient C_f in the channel for simulations with isothermal walls.

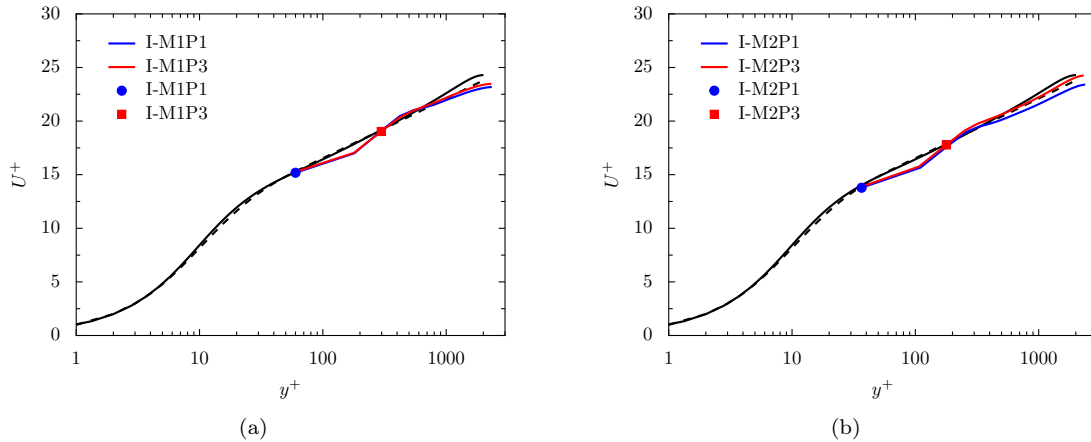


Figure 16. Representation of the mean streamwise velocity obtained from the WMLES for isothermal walls using (a) the mesh M1 and (b) the mesh M2, using the matching point — P1 and — P3; — from the DNS of Hoyas and Jiménez,³² and --- from Reichardt's law, as a function of the wall distance using wall units. The symbols represent the positions of the matching point.

indicating that the temperature gradient at the wall has not a considerable influence on the velocity for this flow regime. The matching points, represented using symbols in figure 6, match with Reichardt's law in dashed line. Selecting the matching point as the third computational point above the wall P3 improves the quality of the results. In particular, the LES using the refined mesh M2 and the matching point P3 shows the best agreement with the DNS and Reichardt's law.

The mean temperature profiles are displayed in figure 17. They are compared to the profile predicted by Kader's law, represented in dashed lines and computed from the friction coefficient and the wall heat flux provided by the empirical correlations of Petukhov³³ and Sleicher and Rouse.³⁴ The matching points are represented by symbols. They are located on the wall law profile, as expected from the definition of the matching point. The influence of the location of the matching point for the LES using the mesh M1 and the mesh M2 is presented in figures 17(a) and 17(b) respectively. The less satisfactory trends are

obtained from the simulation using the mesh M2 and the matching P1. In this simulation, the position of the matching point, at $y_M^+ = 30$, corresponds to the beginning of the logarithmic region and is far from the value of $y_M^+ = 100$ generally recommended for WMLES. The matching point may be too close to the wall to successfully apply WMLES, especially when thermal effects have to be taken into account. The LES using the matching point P3 and the mesh M2 provides the best agreement with Kader's law. These results are comparable to those obtained in the case of an adiabatic wall. In particular, using a relatively well-refined mesh ensures a better resolution of the outer part of the boundary layers, and selecting the matching point P3 allows to respect the recommendations for the matching point location, with $y_M^+ = 150$. Finally, when the point P3 is the matching point, the temperature at the first computational point above the wall P1 remains close to Kader's profile.

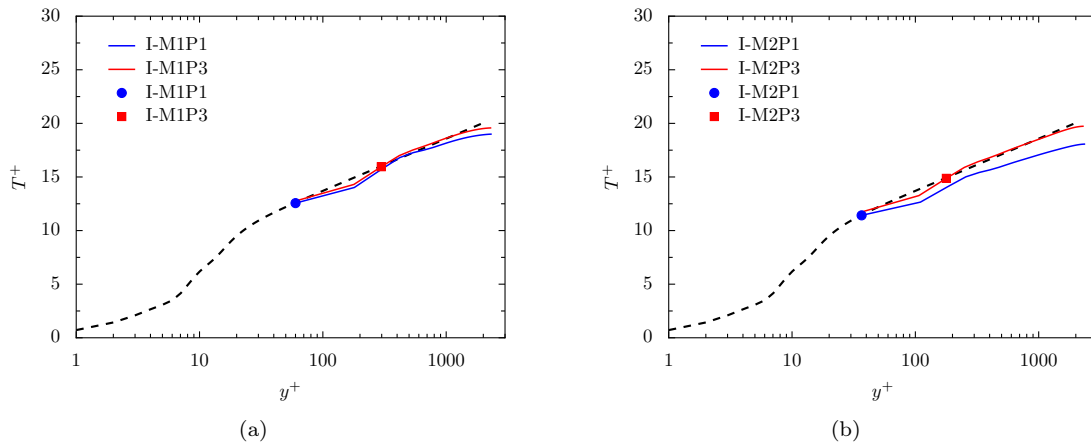


Figure 17. Representation of the mean temperature obtained from the WMLES for isothermal walls using (a) the mesh M1 and (b) the mesh M2, using the matching point — P1 and — P3; and --- from Kader's law, as a function of the wall distance using wall units. The symbols represent the positions of the matching point.

The WMLES approach, successfully applied to turbulent channel flows, is now used to study an isothermal round jet at high Reynolds number.

C. Isothermal subsonic jet

1. Parameters

A subsonic isothermal jet originated from a pipe nozzle is now simulated by LES using the wall model presented above. The jet has a Mach number of $M = u_j/c = 0.6$ and a Reynolds number of $Re_D = u_j D/\nu = 5.7 \times 10^5$, corresponding to the conditions in the experiment of Cavalieri et al.,³⁵ where D and u_j represent the jet diameter and velocity. The ambient pressure P_0 and temperature T_0 are respectively equal to 10^5 Pa and 298 K. The nozzle, illustrated in figure 18, has a length of $L = 0.75D$. At the nozzle exit, located at $z = 0$, the flow is characterized by a boundary-layer thickness of $\delta = 8.5 \times 10^{-2}D$ and a Reynolds number of $Re_\theta = u_j \delta/\nu = 4.5 \times 10^3$, based on the momentum thickness of $\delta_\theta = 7.9 \times 10^{-3}D$. The nozzle lip thickness, at $z = 0$, is equal to $d_{LIP} = 0.006D$.

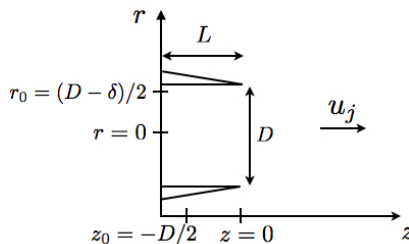


Figure 18. Sketch of the jet nozzle, where D and u_j are the jet diameter and velocity, L is the nozzle width, δ is the boundary-layer thickness, and (z_0, r_0) is the position where the perturbations are injected to trigger the boundary-layer transition toward turbulence.

2. Computational set-up and methods

The wall model approach developed for adiabatic walls in section III.A. is applied inside the nozzle. The third computational point above the wall is chosen to be the matching point. The computational domain for the simulation is represented in figure 19. It extends axially from $z = -0.75D$ down to $z = 33D$, and radially from $r = 0D$ out to $r = 12D$. At the outlet of the domain, Navier-Stokes characteristic boundary conditions³⁶ are prescribed. Tam and Webb radiation conditions³⁷ are used at the inlet boundary and at the lateral sides. Sponge layers are also added to damp the aerodynamic fluctuations and minimize reflections at the domain boundaries. Therefore, the physical domain of the simulation, delimited by dashed lines in figure 19, ends at $z = 25D$ in the axial direction, and at $r = 6D$ in the radial direction.

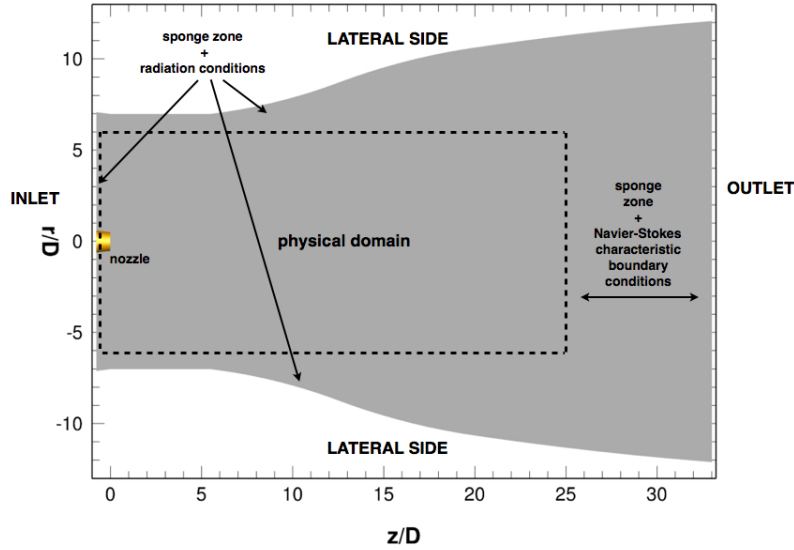


Figure 19. Representation of the computational domain in the (z, r) plane. The physical domain is delimited by dashed lines.

The axial and the radial mesh spacings of the LES grid, denoted Δz and Δr , are respectively shown in figures 20(b) and 20(a). The minimum grid spacings Δr_{min} and Δz_{min} are located at the nozzle lip, with $\Delta r_{min} = d_{LIP}/4$ yielding $\Delta r_{min} = 0.0015D$, and $\Delta z_{min} = 0.0079D$. In the radial direction, the minimum grid spacing corresponds to a value of $\Delta r_{min}^+ \simeq 40$ in wall units. As a result, the matching point for the present wall model approach is located at a distance of $r_M^+ \simeq 100$ from the wall. From the pipe lip, the mesh is progressively stretched with rates which remain lower than 4% in the physical domain to avoid spurious numerical waves to be generated. In particular, in the radial direction, the boundary-layer thickness is discretized by about 20 points at the nozzle exit. In addition, the radial and axial maximum mesh spacings are respectively equal to $\Delta r_{max} = 0.086D$ and $\Delta z_{max} = 0.097D$ in the physical domain. The maximum mesh size Δz_{max} is chosen such that the time frequency f of waves discretized by eight grid points corresponds to the Strouhal number $St = fD/u_j = 2$. In the azimuthal direction, 272 points are equally distributed. Therefore, the computational grid contains 83 million points, including 2.4 million points in the jet pipe.

Initially, the azimuthal and the radial velocity profiles are equal to zero, and the pressure is equal to P_0 . In the pipe, the axial velocity obtained from a preliminary RANS computation is imposed. The temperature is calculated using a Crocco-Busemann relation. In order to seed the laminar-turbulent transition of the flow in the nozzle, vortex rings are added to the flow field in the boundary layers inside the pipe at each time step during the computation.³⁸ The small disturbances are introduced close the nozzle exit, at $r_0 = (D - \delta)/2$ and $z_0 = -D/2$. They are divergence-free to minimize the production of acoustic waves.

The initialization time is equal to $t = 300D/c$. It corresponds to 8 acoustic wave passings through the computational domain in the axial direction. The velocity components and the pressure are recorded during $t = 200D/c$. The flow statistics are averaged in the azimuthal direction. The acoustic propagation to the far-field region is carried out using a Ffowcs-Williams and Hawkins (FW-H) analogy.³⁹ For the far-field extrapolation, the LES data are collected on a cylindrical surface located at $r=2D$. These data are then propagated during a period $50D/c$ to the distance $r = 35D$ from $z = r = 0$. The pressure fluctuations are

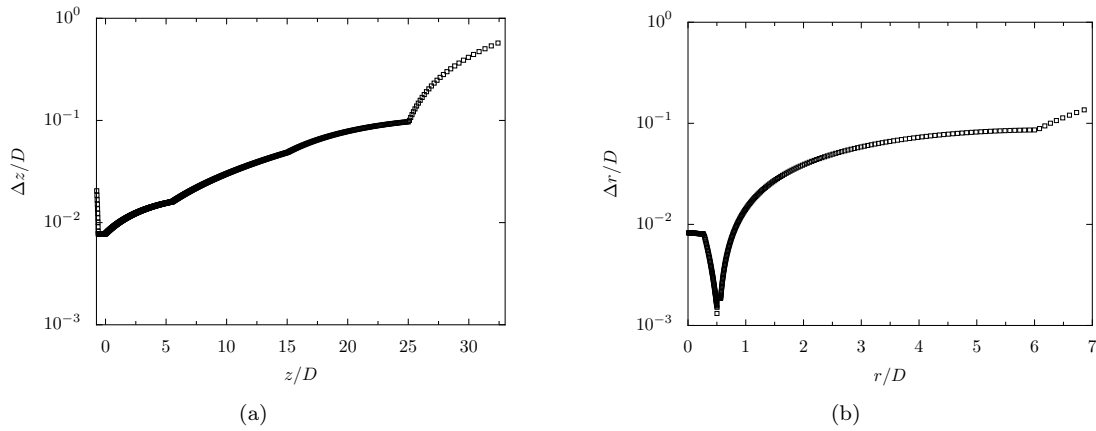


Figure 20. Representation of the mesh spacings: (a) axial mesh spacing $\Delta z/D$ at $r = 0$, (b) radial mesh spacing $\Delta r/D$ at $z = 0.5D$.

then collected during $200D/c$, at a sampling frequency allowing the spectra to be computed up to a Strouhal number of 10.

In order to assess the influence of wall modeling in the present LES, the results of a LES of the present jet flow performed without wall modeling are also presented for comparisons. This LES was carried out using the computational grid previously described. A slip condition was imposed at the solid boundaries. The flow statistics have been collected during a period of $150D/c$, and the pressure fluctuations from the FW-H analogy during a period of $200D/c$.

3. Results

NOZZLE EXIT CONDITIONS In order to characterize the initial conditions of the jet exiting from the pipe, the mean and rms axial velocity profiles at the nozzle exit are represented in figures 21(a) and 21(b). In addition, flow parameters at the pipe exit, including the boundary-layer thickness δ , the momentum thickness δ_θ , and the maximum value of the rms axial velocity are given in table 7. Mean turbulent velocity profiles $\langle u_z \rangle$ are in good agreement with the measurements for the simulations with and without wall modeling. In particular, the boundary-layer thicknesses differ by less than 5% difference from the measurements in both simulations. The LES with wall modeling yields a momentum thickness of $\delta_\theta = 0.0081D$ which is very close to the experimental value of $0.0079D$. The rms axial velocity at the nozzle exit are correctly predicted when wall modeling is applied inside the pipe. More precisely, their shapes are comparable with the profiles measured by Cavalieri et al.³⁵ A rms peak around 14% of the jet velocity is obtained, which is comparable with the experimental value of 11%. When no wall model is applied, however, the intensity of the rms peak is overestimated compared to the experiment and shows a peak magnitude of $\langle u_z'^2 \rangle^{1/2} = 0.20u_j$.

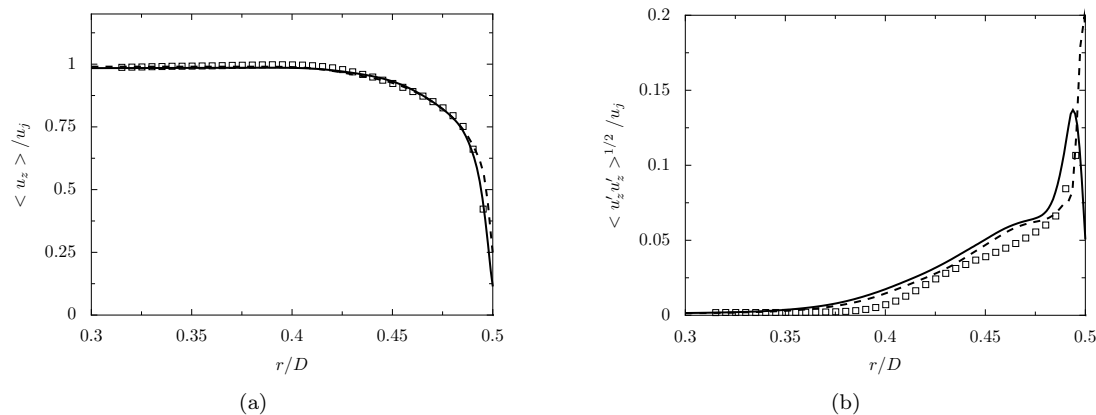


Figure 21. Representation of (a) the mean axial velocity and (b) the rms axial velocity at the nozzle exit of the jet, — from WMLES, - - - from LES without wall modeling, and $\square \square$ from the results of the experiment of Cavalieri et al.³⁵

	δ/D	δ_θ/D	$\max(\langle u'_z u'_z \rangle^{1/2} / u_j)$
WMLES	0.082	0.0081	0.14
LES	0.086	0.0084	0.20
EXP (Reference)	0.085	0.0079	0.11

Table 7. Nozzle exit conditions at $z = 0$, where δ is the boundary-layer thickness, δ_θ is the momentum thickness, and $\max(\langle u'_z u'_z \rangle^{1/2} / u_j)$ is the maximum value of the rms axial velocity.

JET DEVELOPMENT The aerodynamical development of the jet is illustrated in figure 22 where the instantaneous vorticity field for the wall-modeled LES is represented. Downstream of the nozzle lip at $z = 0$, the shear layer thickness increases and the mixing layers merge around $z = 6D$, indicating the end of the potential core. Small turbulent structures, colored in red and typical of flows at high Reynolds numbers, are visible.

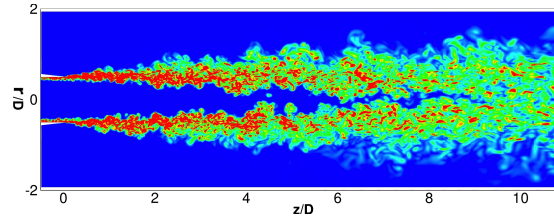


Figure 22. Snapshot of the vorticity modulus from WMLES in the (z, r) plane using color levels between 0 and $10u_j/D$, from blue to red.

More quantitative results concerning the jet development are provided in figures 23 and 24 where the mean and rms axial velocity are displayed at $z = 1D$ and $z = 5D$. The development of the jet at $z = 1D$ and at $z = 5D$ are comparable for the LES with and without wall modeling. In particular, the mean velocity profiles show a good agreement with the measurements. At $z = 1D$, the fluctuating velocity profiles are close to the experimental values and reach a maximum value around $0.175u_j$. A slight over-estimation of the width of the rms peak is observed compared to the experimental data. At $z = 5D$, the rms profiles agree well with the measurements near the jet centerline, whereas lower turbulent levels are observed for $r \geq 0.3D$.

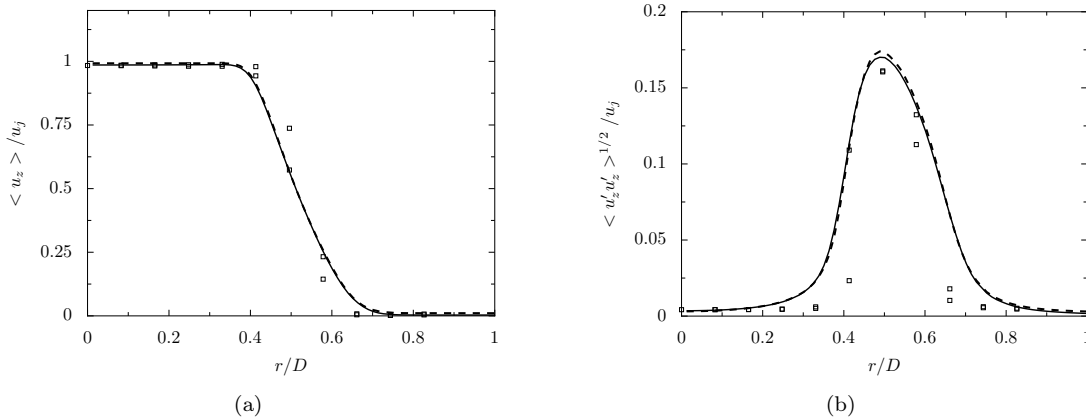


Figure 23. Representation of (a) the mean axial velocity and (b) the rms axial velocity at $z = 1D$, — from WMLES, --- from LES without wall modeling, and $\square \square \square$ from the results of the experiment of Cavalieri et al.³⁵

FAR-FIELD NOISE In order to quantify the acoustic levels radiated from the jet in the far-field region, the pressure spectra computed at $r = 35D$ from the nozzle are presented in figure 25 for the emission angles of $\phi = 30^\circ$ and $\phi = 90^\circ$ relative to the flow direction. A very good agreement with the experimental results is obtained from the simulation using wall modeling. More precisely, the sound levels predicted by the wall-modeled LES are close to the measurements up to the Strouhal number of $St = 2$, corresponding to the cut-off frequency of the mesh. In particular, both the intensity and the position of the peak around $St = 0.25$ are well-captured at both angles. The LES without wall modeling provides stronger sound levels

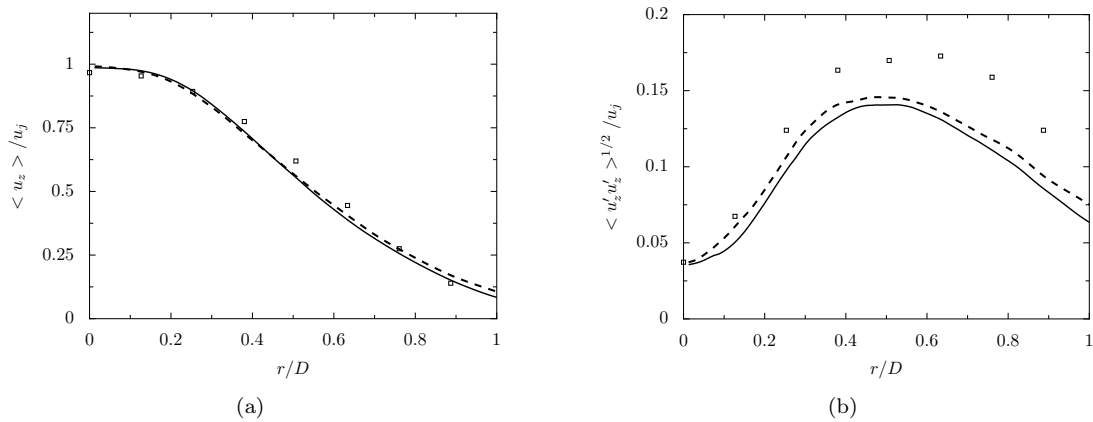


Figure 24. Representation of (a) the mean axial velocity and (b) the rms axial velocity at $z = 5D$, — from WMLES, --- from LES without wall modeling, and $\square \square$ from the results of the experiment of Cavalieri et al.³⁵

than WMLES. In particular, noise is over-estimated by 5 dB in the spectra at 90° . These results demonstrate the advantage of using LES with wall modeling to predict the noise levels radiated by the jet.

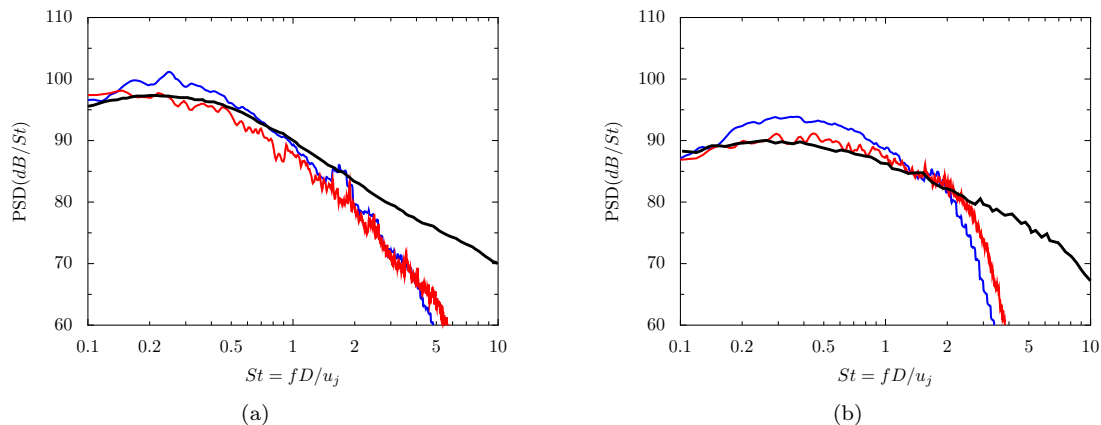


Figure 25. Representation of the pressure spectra at a distance of $35D$ from the nozzle for the angles (a) $\phi = 30^\circ$ and (b) $\phi = 90^\circ$ from the jet direction, as a function of the Strouhal number St : — WMLES, — LES without wall modeling, and — results of the experiment of Cavalieri et al.³⁵

IV. Conclusions

In this paper, a numerical procedure is presented to perform LES of wall-bounded flows using high-order implicit schemes. A spatial discretization is proposed to apply the 6th-order seven-point stencil schemes at the walls. This approach is validated by computing a bi-periodic turbulent channel flow at a Reynolds number of $Re_\tau = 395$. In this case, the results agree very well with DNS data, which demonstrates that the LES algorithm, based on the use of a selective filter as a subgrid-scale model, can be applied to compute wall-bounded turbulent flows. For flows at high Reynolds numbers, an analytical wall model is coupled with the high-order schemes to perform LES at an acceptable computational cost. The performance of the wall-modeled LES approach is first examined for a bi-periodic turbulent channel flow at $Re_\tau = 2000$. The results show a good agreement with DNS data. A subsonic isothermal round jet at $Re_\tau = 5.7 \times 10^5$ is then simulated, using wall modeling inside the jet nozzle. The wall-modeled LES approach is found to significantly improve the results for the jet flow and the noise radiated in the far-field regions, compared to a LES performed without wall modeling on the nozzle wall. In particular, when using wall modeling, the jet nozzle exit conditions are closer to the experimental data. For the far-field noise spectra, a better agreement with the measurements is reported. The results presented in this paper illustrate the capability of the wall modeled-LES approach to predict the noise radiated from jet flows at high Reynolds numbers.

Acknowledgments

This study is supported by Airbus. This work was granted access to the HPC resources of CINES under the allocation 2015-[x20152a6074] made by GENCY. The postprocessing was performed using Antares.⁴⁰

References

- ¹T Colonius and SK Lele. Computational aeroacoustics: progress on nonlinear problems of sound generation. *Progress in Aerospace sciences*, 40(6):345–416, 2004.
- ²H Choi and P Moin. Grid-point requirements for large eddy simulation: Chapman’s estimates revisited. *Annual Research Briefs (Center for Turbulence Research)*, pages 31–36, 2011.
- ³C Bogey and C Bailly. Influence of nozzle-exit boundary-layer conditions on the flow and acoustic fields of initially laminar jets. *Journal of Fluid Mechanics*, 663:507–538, 2010.
- ⁴C Bogey and O Marsden. Identification of the effects of the nozzle-exit boundary-layer thickness and its corresponding Reynolds number in initially highly disturbed subsonic jets. *Physics of Fluids*, 25(5):055106, 2013.
- ⁵U Piomelli and E Balaras. Wall-layer models for large-eddy-simulations. *Annual Review of Fluid Mechanics*, 34:349–374, 2002.
- ⁶J Slotnick, A Khodadoust, J Alonso, D Darmofal, W Gropp, E Lurie, and D Mavriplis. CFD vision 2030 study: A path to revolutionary computational aerosciences. 2014.
- ⁷JW Deardorff. A numerical study of three-dimensional turbulent channel flow at large reynolds numbers. *Journal of Fluid Mechanics*, 41(2):453–480, 1970.
- ⁸U Schumann. Subgrid scale model for finite difference simulations of turbulent flows in plane channels and annuli. *Journal of Computational Physics*, 18(4):376–404, 1975.
- ⁹S Kawai and J Larsson. Wall-modeling in large eddy simulation: Length scales, grid resolution, and accuracy. *Physics of Fluids*, 24:015105, 2012.
- ¹⁰G Lodato, P Castonguay, and A Jameson. Structural wall-modeled LES using a high-order spectral difference scheme for unstructured meshes. *Flow, Turbulence and Combustion*, 92(1-2):579–606, 2014.
- ¹¹A Fosso. *Schémas Volumes Finis Précis*. PhD thesis, Université Pierre et Marie Curie, 2011.
- ¹²S Bocquet, P Sagaut, and J Jouhaud. A compressible wall model for large-eddy simulation with application to prediction of aerothermal quantities. *Physics of Fluids*, 24:065103, 2012.
- ¹³L Cambier, S Heib, and S Plot. The Onera Elsa CFD Software: Input from Research and Feedback from Industry. *Mechanics & Industry*, 14(03):159–174, January 2013.
- ¹⁴A Fosso, H Deniau, F Sicot, and P Sagaut. Curvilinear finite volume scheme using high order compact interpolation. *Journal of Computational Physics*, 229(13):5090–5122, 2010.
- ¹⁵SK Lele. Compact finite difference schemes with spectral-like resolution. *Journal of Computational Physics*, 103:16–42, 1992.
- ¹⁶MR Visbal and DV Gaitonde. On the use of higher-order finite-difference schemes on curvilinear and deforming meshes. *Journal of Computational Physics*, 181:155–185, 2002.
- ¹⁷M Lazareff, AM Vuillot, and L Cambier. Manuel théorique du logiciel elsA, 2010.
- ¹⁸C Bogey and C Bailly. A family of low dispersive and low dissipative explicit schemes for flow and noise computations. *Journal of Computational Physics*, 194(1):194–214, 2004.
- ¹⁹A Fosso, H Deniau, N Lamarque, and T Poinsot. Comparison of outflow boundary conditions for subsonic aeroacoustic simulations. *International Journal for Numerical Methods in Fluids*, 68(10):1207–1233, 2012.
- ²⁰A Fosso Pouangué, M Sanjosé, S Moreau, G Daviller, and H Deniau. Subsonic jet noise simulations using both structured and unstructured grids. *AIAA Journal*, 53(1):55–69, 2014.
- ²¹MH Carpenter, D Gottlieb, and S Abarbanel. Time-stable boundary conditions for finite-difference schemes solving hyperbolic systems: methodology and application to high-order compact schemes. *Journal of Computational Physics*, 111(2):220–236, 1994.
- ²²TK Sengupta, G Ganeriwal, and S De. Analysis of central and upwind compact schemes. *Journal of Computational Physics*, 192:677–694, 2003.
- ²³H Abe, H Kawamura, and H Choi. Very large-scale structures and their effects on the wall shear-stress fluctuations in a turbulent channel flow up to $Re_\tau = 640$. *Journal of Fluids Engineering*, 126(5):835–843, 2004.
- ²⁴RD Moser, J Kim, and NN Mansour. Direct numerical simulation of turbulent channel flow up to $Re_\tau = 590$. *Physics of Fluids*, 11:943, 1999.
- ²⁵H Abe, H Kawamura, and Y Matsuo. Direct numerical simulation of a fully developed turbulent channel flow with respect to the Reynolds number dependence. *Journal of Fluids Engineering*, 123(2):382–393, 2001.
- ²⁶O Cabrit. Direct simulations for wall modeling of multicomponent reacting compressible turbulent flows. *Physics of Fluids*, 21:055108, 2009.
- ²⁷F Kremer. *Étude numérique d’écoulements de paroi compressibles: méthodes d’intégration temporelle semi-implicites et application du canal plan turbulent*. PhD thesis, École Centrale de Lyon, 2012.
- ²⁸H Reichardt. The fundamentals of turbulent heat transfer. *Archiv fuer die Gesamte Waermetechnik, (West Germany)*, 6:129–143, 1951.
- ²⁹BA Kader. Temperature and concentration profiles in fully turbulent boundary layers. *International Journal of Heat and Mass Transfer*, 24(9):1541–1544, 1981.

- ³⁰ER Van Driest. Turbulent boundary layer in compressible fluids. *Journal of the Aeronautical Sciences*, 18(3):145–160, 1951.
- ³¹KM Aikens, NS Dhamankar, CS Martha, Yingchong S, GA Blaisdell, AS Lyrantzis, and Z Li. Equilibrium wall model for large eddy simulations of jets for aeroacoustics. 2014.
- ³²S Hoyas and J Jiménez. Scaling of the velocity fluctuations in turbulent channels up to $Re_\tau = 2003$. *Physics of Fluids*, 18:011702, 2006.
- ³³BS Petukhov. Heat transfer and friction in turbulent pipe flow with variable physical properties. *Advances in heat transfer*, 6:503–565, 1970.
- ³⁴CA Sleicher and MW Rouse. A convenient correlation for heat transfer to constant and variable property fluids in turbulent pipe flow. *International Journal of Heat and Mass Transfer*, 18(5):677–683, 1975.
- ³⁵AVG Cavalieri, P Jordan, T Colonius, and Y Gervais. Axisymmetric superdirectivity in subsonic jets. *Journal of Fluid Mechanics*, 704:388–420, 2012.
- ³⁶T Poinso and SK Lele. Boundary conditions for direct simulations of compressible viscous flows. *Journal of Computational Physics*, 101(1):104–129, 1992.
- ³⁷CKW Tam and JC Webb. Dispersion-relation-preserving finite difference schemes for computational acoustics. *Journal of Computational Physics*, 107:262–281, 1993.
- ³⁸C Bogey, C Bailly, and D Juvé. Noise investigation of a high subsonic, moderate reynolds number jet using a compressible large eddy simulation. *Theoretical and Computational Fluid Dynamics*, 16(4):273–297, 2003.
- ³⁹D Casalino. An advanced time approach for acoustic analogy predictions. *Journal of Sound and Vibration*, 261(4):583–612, 2003.
- ⁴⁰A Gomar, T Léonard, et al. Antares: Python Post-Processing Library, Centre Européen de Recherche et de Formation Avancée en Calcul Scientifique (CERFACS), Toulouse, France, 2012.